UDK 669.14:66.022.5
Original scientific article/Izvirni znanstveni članek

ISSN 1580-2949
MTAEC9, 56(1)65(2022)

RESIDUAL STRESS MODELING AND ANALYSIS IN AISI A2 STEEL PROCESSED BY AN ELECTRICAL DISCHARGE MACHINE

MODELIRANJE ZAOSTALIH NAPETOSTI IN ANALIZA JEKLA VRSTE AISI A2, OBDELANEGA S POTOPNO EROZIJO

Dinesh Kumar[1,*], Krishan Kant Singh Mer[2], Hoshiyar Singh Payal[3], Kapil Kumar[4]

[1]Department of Mechanical Engineering, Institute of Technology, Gopeshwar, Uttarakhand, India, 246424
[2]Institute of Technology, Gopeshwar, Uttarakhand, India, 246424
[3]Department of Mechanical Engineering, SRHU Dehradun, Uttarakhand, India, 248001
[4]Department of Mechanical Engineering, THDC – Institute of Hydropower Engineering & Technology, Tehri-Garhwal, Uttarakhand, India, 249001

Prejem rokopisa – received: 2021-11-27; sprejem za objavo – accepted for publication: 2021-12-31

doi:10.17222/mit.2021.325

Due to the creation of a significant temperature gradient, electrical discharge machining (EDM) causes localized, high thermal stress in a tiny heat-affected zone. This thermally developed stress leads to fatigue life and strength decrement, micro-cracks and probably catastrophic failure. On AISI A2 steel, a mathematical model based on finite-element analysis was constructed to estimate the temperature field and associated thermal stresses. In this present research work, the heat-flux distribution in a single spark during EDM is considered to be Gaussian distributed. The model first calculates the temperature distribution, and then uses this temperature field to determine the thermal stresses. It was observed that the stresses surpass the workpiece material's yield strength near the center of the spark and this gradually weakens as the distance from the center increases.

Keywords: electrical discharge machining, numerical simulation, residual stress, AISI A2 die steel, Gaussian distribution, heat flux

Zaradi nastanka močnega temperaturnega gradienta med mehansko obdelavo z elektro erozijo (EDM; angl.: Electro Discharge Machining) prihaja do nastanka lokalnih termičnih napetosti v nastali, relativno ozki, toplotno vplivani coni. Nastale napetosti, zaradi toplotnega gradienta, povzročajo utrujanje materiala, ki vodi do zmanjšanja njegove trajne trdnosti oz. dobe trajanja zaradi nastanka mikro-razpok, kar lahko v končni konsekvenci privede do katastrofalne porušitve materiala oz. strojnega dela iz katerega je le ta izdelan. Avtorji v članku opisujejo izdelavo matematičnega modela za jeklo vrste AISI A2, ki temelji na analizi s pomočjo metode končnih elementov. Z matematičnim modelom so lahko ocenili nastalo temperaturno polje in z njim povezane termične napetosti. V raziskavi avtorji porazdelitev toplotnega toka obravnavajo kot Gaussovo porazdelitev med eno samo izmenično razelektritvijo (oblokom), ki poteka med EDM. S pomočjo modela so izračunali porazdelitev temperature in nato s pomočjo ugotovljenega temperaturnega polja določili termične napetosti. Avtorji v članku ugotavljajo, da nastale napetosti presegajo mejo plastičnosti preiskovanega materiala (AISI A2) v bližini centra obloka in se le te postopoma zmanjšujejo z oddaljevanjem od njegovega središča.

Ključne besede: mehanska obdelava z električno potopno erozijo, numeričnasimulacija, zaostale napetosti, orodno jeklo vrste AISI A2, Gaussova porazdelitev toplotnega toka

1 INTRODUCTION

Electrical discharge machining (EDM) is a thermal machining process in which the discharge channel creates thermal energy. The resulting thermal energy in the discharge channel causes melting of the work piece and evaporation thereafter. Thermal energy discharge with a high density results in high temperatures being generated, which leads to thermal erosion and micro-cracks on the recast layer of the workpiece surface. The formation of the heat-affected zone in multi-layered recast layer and hardened surface brittleness leads to a fatigue-strength reduction of the work piece.[1–3] So it is wiser to calculate the temperature distribution and then the thermal stresses in the work piece.

Klink et al. investigated the residual stress distribution on a wire-EDM-machined subsurface of ASP 23 tool steel. They found a high tensile residual stress zone about 30 mm beneath the material's surface.[4] In the wire-EDM of Ni and Ti alloys, Atar et al. reported a similar pattern.[5] Wire-EDMed Udimet 720 components exhibited a much higher tensile residual stress on the surface and a short fatigue life, whereas milled parts had surface compressive stresses and a substantially longer fatigue life.[6]

Erden et al. gives a broad review of EDM mathematical models, which are based on a crater-formation phenomenon with a single spark. Wider and larger efforts are made so far for the estimation of the machined surface profile, crater volume, tool wear rate (TWR) and material removal rate (MRR). But the models that are useful to estimate the machined component's surface integrity are still scarce.[7] The surface-integrity models are

*Corresponding author's e-mail:
dineshmmm@gmail.com (Dinesh Kumar)

primarily based on a metallurgical analysis of EDM surfaces utilizing various experimental techniques such as scanning electron microscopy (SEM), optical metallography, and X-ray diffraction.[8–10] Kruth et al. found that the electricalde and work-piece materials, as well as the kind of dielectric, had an effect on the metallographic phase of the white layer.[2] A review of the available literature reveals that there are very few theoretical techniques for determining the thermal stress.

The thermal energy generated in the EDM process influences the surface integrity of the machined work piece. So, it is very important to compute the temperature and thermal stress distribution in the machined components. In this context, firstly the temperature distribution in the machined component is computed and analyzed, and then the thermal stress due to a non-uniform distribution of temperature is estimated and the machined component is analyzed to determine the thermal residual stresses. The thermal residual stresses directly influences the surface quality.

There is a large literature on the thermo-mathematical modelling of the EDM process, which describes an excellent correlation with experimental results.[11,12]

In the present work, the finite-element technique is used to model the thermal stress due to EDM. The designed model is to predict the thermal stress that will occur. To find out the developed thermal stress in the machined component during EDM, firstly the temperature distribution is calculated and then uses this temperature field to determine the thermal stresses. The temperature field is calculated using a temperature model that considers the heat flow magnitude and distribution.

2 MODELING

In EDM, the tool and workpiece are completely submerged and maintained at a gap, known as the inter-electrode gap in dielectric solution. Due to the complexity of the EDM process the following assumptions are made:

1) The workpiece material is isotropic and homogeneous.
2) About r-z plane, the domain is axisymmetric.
3) The properties of the workpiece material are independent of the temperature.
4) The heat transfer is carried out by convection process.
5) The analysis is made only for one spark.
6) The workpiece is stress free before the EDM process.
7) During a phase change the latent heat of the material is not considered.
8) Body force effects and inertia are negligible during the process of stress development.
9) Thermal stress is only analyzed up to the time when the transient temperature distribution above dielectric temperature is known.
10) The workpiece material is elastic-perfectly plastic, with a yield strength in tension equal to that in compression.

2.1 Modeling of temperature

2.1.1 Governing equations

In an axisymmetric domain, the single spark heating of a workpiece is considered. So, the heating of the workpiece is governed by the thermal diffusion differential Equation (1):

$$\rho C \frac{\partial T}{\partial t} = \frac{1}{r}\frac{\partial}{\partial r}\left(k\frac{\partial T}{\partial r}\right) + \frac{\partial}{\partial z}\left(k\frac{\partial T}{\partial z}\right) \quad (1)$$

where ρ is density, C is specific heat capacity in the solid state of the workpiece, T is temperature, t is time, k is thermal conductivity, r and z are cylindrical coordinates.

2.1.2 Boundary conditions

For spark domain, a cylindrical small portion of the workpiece is considered. Heat input from a single spark serves to maintain the condition of a thermal boundary over the uppermost surface Γ_1. The heat transmitted by the coolant on the upper layer Γ_1 is modeled as a convective boundary condition. The boundaries Γ_2, Γ_3 and Γ_4 are so far apart that no heat transmission occurs across them. The boundary Γ_4 is a symmetric axis. As a result, the boundary conditions are as follows:

$$k\frac{\partial T}{\partial r} = \begin{cases} h(T - T_0) & if r > R \\ q & \text{if } r \le R \text{ on } \Gamma_1 \\ 0 & f \text{ or } off \text{ time} \end{cases} \quad (2)$$

$$\text{For } \Gamma_2, \Gamma_3 \text{ and } \Gamma_4, \ \partial T/\partial n = 0 \quad (3)$$

where q is the entering heat flux inflowing inside the workpiece, the heat-transfer coefficient is denoted by h, R is the spark radius, T_0 is the room temperature and n is the normal to the boundary.

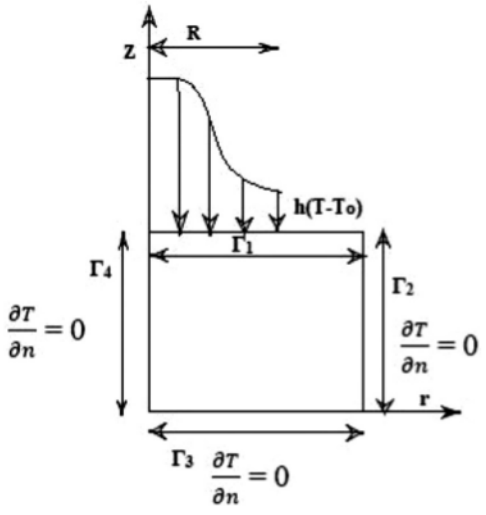

Figure 1: Thermal model of EDM

2.1.3 Radius of spark (R)

The spark radius is determined by the electricalde material, and measuring spark radius is challenging due to the extremely high pulse frequency. Shankar et al. used an integrated approach model to determine the spark shape to be non-cylindrical.[13] Most researches proposed empirical formula for calculating the spark radius.[14–17] As per a literature review, there is a shortage of thorough information for evaluating its size and shape. The spark radius in this study was computed using Shankars et al.'s result as

$$R = ZP^m T^n \tag{4}$$

P denotes discharge power, T denotes time, while Z, m, and n denote empirical constants.

For the current workpiece material and the dielectric combination under consideration, it is recommended that, because power is a function of I_p, the radius of spark can be calculated by altering Equation (3).

$$R = ZI_p^m T_{on}^n \tag{5}$$

where I_p is the discharge current, T_{on} is the pulse on time and the empirical constants Z = 325, m = 0.55, and n = 0.247 are used, and the spark radius can be written as:

$$R = 325 I_p^{0.55} T_{on}^{0.247} \tag{6}$$

2.1.4 Heat flux by a single spark

The shape of the crater produced during EDM suggested a non-uniform dispersion of a spark's heat source. In the present paper, a Gaussian heat-flux distribution is assumed.[18,19] The heat flux q_w at radius r is presented in Equation (7).

$$q_w(r) = q_0 \exp\left\{-4.5\left(\frac{r}{R}\right)^2\right\} \tag{7}$$

The maximum intensity q_o at the spark axis and its radius R are known.

If one spark used the total power of each pulse then

$$q_w(r) = \frac{4.45 R_w U_b I}{\pi R^2} \exp\left\{-4.5\left(\frac{r}{R}\right)^2\right\} \tag{8}$$

where U_b is the discharge voltage or breakdown voltage, R_w is the energy partition to the work piece and I is the current.

2.1.5 Energy partition R_w

The energy partition R_w is the proportion of the distributed input heat spread across the anode, cathode, and dielectric. It is determined by the material characteristics of the individual electrodes. Many researchers proposed values of energy partition R_w during EDM process, but no thorough technique for calculating the value of the energy partition R_w has been discovered yet during the EDM process. In this work the energy partition R_w is set at 0.08.[20,21]

2.2 Modeling of thermal stress

The thermal stresses in the workpiece are generated by an extreme temperature gradient during the EDM process. The transient distribution of temperature in the work piece, as well as the boundary and initial conditions, are used to calculate the thermal stresses.

2.2.1 Equilibrium equations

In elasticity theory, the equilibrium equations must be satisfied by the stresses in the structure. The force equilibrium of a point is used to generate these Equation (9) and Equation (10).

$$\frac{\partial \sigma_{rr}}{\partial r} + \frac{\partial \sigma_{rz}}{\partial z} + \frac{\sigma_{rr} - \sigma_{\theta\theta}}{\partial r} = 0 \tag{9}$$

$$\frac{\partial \sigma_{rz}}{\partial r} + \frac{\partial \sigma_{zz}}{\partial z} + \frac{\sigma_{rz}}{\partial r} = 0 \tag{10}$$

where σ_{rz} is the shear stress and σ_{rr}, σ_{zz} and $\sigma_{\theta\theta}$ are the normal stresses.

2.2.2 Stress–strain–temperature relations

Because of the temperature rise ΔT, the stress-strain-temperature relationship is

$$\{\varepsilon\} = [D]\{\varepsilon\} - \{m\} \tag{11}$$

where $\{\sigma\}$ is the stress vector, $\{\varepsilon\}$ is the strain vector and $[D]$ is the elasticity matrix.

$$\{\sigma\}^T = \{\sigma_{rr}, \sigma_{zz}, \sigma_{\theta\theta}, \sigma_{rz}\} \tag{12}$$

$$\{\varepsilon\}^T = \{\varepsilon_{rr}, \varepsilon_{zz}, \varepsilon_{\theta\theta}, \varepsilon_{rz}\} \tag{13}$$

$$\{m\} = \begin{Bmatrix} 1 \\ 1 \\ 1 \\ 0 \end{Bmatrix} \frac{E\alpha_t \Delta T}{1-2\nu} \tag{14}$$

where α_t is the coefficient of thermal expansion, E is the Young's modulus and ν is the Poisson's ratio.

$$[m] = \frac{E}{(1+\nu)(1-2\nu)} \begin{bmatrix} 1-\nu & \nu & \nu & 0 \\ \nu & 1-\nu & \nu & 0 \\ \nu & \nu & 1-\nu & 0 \\ 0 & 0 & 0 & \frac{1-2\nu}{2} \end{bmatrix} \tag{15}$$

Because of the temperature rise ΔT, the final stress-strain-temperature relationship can be represented as

$$\begin{Bmatrix} \sigma_{rr} \\ \sigma_{\theta\theta} \\ \sigma_{zz} \\ \sigma_{rz} \end{Bmatrix} = \frac{E}{(1+\nu)(1-2\nu)} \begin{bmatrix} 1-\nu & \nu & \nu & 0 \\ \nu & 1-\nu & \nu & 0 \\ \nu & \nu & 1-\nu & 0 \\ 0 & 0 & 0 & \frac{1-2\nu}{2} \end{bmatrix} \cdot \begin{Bmatrix} \varepsilon_{rr} \\ \varepsilon_{\theta\theta} \\ \varepsilon_{zz} \\ \varepsilon_{rz} \end{Bmatrix} - \begin{Bmatrix} 1 \\ 1 \\ 1 \\ 0 \end{Bmatrix} \frac{E\alpha_t \Delta T}{1-2\nu} \tag{16}$$

2.2.3 Strain displacement relations

$$\varepsilon_{rr} = \frac{\partial u}{\partial r},\ \varepsilon_{zz} = \frac{\partial w}{\partial z},\ \varepsilon_{\theta\theta} = \frac{u}{r},\ \varepsilon_{rz} = \frac{\partial u}{\partial z} + \frac{\partial w}{\partial r} \quad (17)$$

where u and w are the displacements, ε_{rr}, ε_{zz} and $\varepsilon_{\theta\theta}$ are the normal strain, ε_{rz} is the shear strain.

2.2.4 Plastic zone

The equivalent thermal stress in the plastic zone is larger than the yield strength of the material and this point is recognized by the inequality as:

$$\sigma_{eq} \geq \sigma_y \quad (18)$$

The deviatoric stress components are:

$$S_{rr} = \sigma_{rr} - \frac{1}{3}(\sigma_{rr} + \sigma_{zz} + \sigma_{\theta\theta}) \quad (19)$$

$$S_{\theta\theta} = \sigma_{\theta\theta} - \frac{1}{3}(\sigma_{rr} + \sigma_{zz} + \sigma_{\theta\theta}) \quad (20)$$

$$S_{zz} = \sigma_{zz} - \frac{1}{3}(\sigma_{rr} + \sigma_{zz} + \sigma_{\theta\theta}) \quad (21)$$

The effective or equivalent stress is:

$$S_{eq} = \sqrt{3J_2} \quad (22)$$

where J_2 is:

$$J_2 = \frac{1}{2}(S_{rr}^2 + S_{zz}^2 + S_{\theta\theta}^2) + S_{rz}^2 \quad (23)$$

2.2.5 Boundary conditions

In **Figure 1** the displacement u and w along and across the surface Γ_4 are supposed to be zero.

$$u = 0 \text{ and } w = 0 \text{ on } \Gamma_3 \quad (24)$$

Because the surface Γ_4 has an axis of symmetry, the shear component of the traction vector t_z and the normal component of the displacement vector u are both zero along the boundary.

$$t_z = 0 \text{ and } u = 0 \text{ on } \Gamma_4 \quad (25)$$

Because surface Γ_2 is far away from the heat source, it is deemed to be stress-free. Thus, the traction components t_r and t_z are zero along the surface Γ_2

$$t_r = 0 \text{ and } t_z = 0 \text{ on } \Gamma_2 \quad (26)$$

Because the surface Γ_1 is a free surface, the traction components t_r and t_z are both zero along the surface Γ_1

$$t_r = 0 \text{ and } t_z = 0 \text{ on } \Gamma_1 \quad (27)$$

The stress tensor σ_{ij} and the traction component t_r and t_z are related as

$$t_i = \sigma_{ij}\, n_i \quad (28)$$

The components of the unit outward normal vector are denoted by n_i.

3 FINITE-ELEMENT ANALYSIS

The temperature and thermal stress distributions due to a single spark's heat flux are calculated using a Galerkin finite-element approach.

3.1 Temperature analysis

When the Galerkin technique is used on the EDM process then the elemental capacitance matrix $[C^c]$

$$[C^c] = \int_{\Omega^e}\int \rho C \{N^e\}\{N^e\}^T r\,dr\,dz \quad (29)$$

Elemental conductivity matrix $[K^e]$

$$[K^e] = \int_{\Omega^e}\int \rho C [B^e]^T [B^e] r\,dr\,dz \quad (30)$$

Boundary conductivity matrix

$$[K^b] = \int_{\Gamma_b}\int r \{N^b\}\{N^b\}^T \,d\Gamma \quad (31)$$

Boundary flux vector

$$[f^b] = \int_{\Gamma_b}\int r \{N^b\}\{N^b\}^T \{q_w^b\}\,d\Gamma \quad (32)$$

where $\{N^e\}$ denotes the shape-function vector for the elemental element and $\{N^b\}$ denotes the shape function vector for the boundary element. $[B^e]$is a matrix that displays derivatives of temperature with their nodal values, where Γ_b is the boundary element domain, Ω^e is the area element domain, and $\{q_w^b\}$ is the vector that contains nodal values of the heat flux.

The preceding equations are numerically calculated using Gaussian quadrature, taking three points in each direction into account. When the elemental quantities of the preceding equations are added together, we get the differential equations shown below.

$$[C]\{\dot{T}\} + [K]\{T\} = \{F\} \quad (33)$$

where $\{T\}$ is the global temperature vector, $\{\dot{T}\}$ is the time derivative of $\{T\}$, $\{F\}$ is the global heat flux vector, $[C]$ is the global capacitance matrix and $[K]$ denotes the global conductivity matrix.

The above differential equations are solved by the finite-difference method. This technique transforms the differential equations listed above into a set of algebraic equations as

$$[A]_{i+1}\{T\} = \{B\}_{i+1} \quad (34)$$

where,

$$[A]_{i+1} = [C] + \theta\, \Delta t_{i+1}\, [K] \quad (35)$$

$$\{B\}_{i,i+1} = \Delta t_{i+1}\, (\theta\, \{F\}_{i+1} + (1 - \theta)\, \{F\}_i) + \\ + ([C] - (1 - \theta)\, \Delta t_{i+1}\, [K])\{T\}_l \quad (36)$$

In present work $\theta = 2/3$ (Galerkin scheme).

The solution of the aforementioned simultaneous algebraic equations yields the nodal temperature at the new time level after each time interval Δt. As a result, the solution follows the time as Δt_1 equals the pulse on

time and Δt_2 equals the pulse off time of EDM until the required end time is reached.

3.2 Residual thermal stress evaluation and analysis

The equilibrium equations will not be fully satisfied by the displacement function. In the overall sense, a set of functions known as weighted functions (w_r and w_z) are utilized to nullify the resulting error in them. Equilibrium equations with a weighted integral expression are expressed as

$$\int\int_{\Omega}\left[\left(\frac{\partial\sigma_{rr}}{\partial r}+\frac{\partial\sigma_{rz}}{\partial z}+\frac{\sigma_{rr}-\sigma_{\theta\theta}}{r}\right)w_r+\left(\frac{\partial\sigma_{rz}}{\partial r}+\frac{\partial\sigma_{zz}}{\partial z}+\frac{\sigma_{rz}}{r}\right)w_z\right]\cdot 2\pi r\mathrm{d}r\mathrm{d}z \tag{37}$$

Applying divergence theorem

$$\int_{\Omega^e}\{\nabla w\}^{\mathrm{T}}\{\sigma\}2\pi r\mathrm{d}r\mathrm{d}z \tag{38}$$

Using the stress-strain-temperature relationship of Equation (11)

$$\int_{\Omega^e}\{\nabla w\}^{\mathrm{T}}([D]\{\varepsilon\}-\{m\})2\pi r\mathrm{d}r\mathrm{d}z \tag{39}$$

A parabolic curve defines the boundaries of isoperimetric elements, eight isoperimetric elements are used for the present analysis. The strain and displacement of each element are

$$\{\varepsilon\} = [\mathrm{B}]\{\delta\}^{\mathrm{e}} \tag{40}$$

$$\{\mathrm{u}\} = [\mathrm{N}]\{\delta\}^{\mathrm{e}} \tag{41}$$

where $[N]$ denotes the shape-function matrix, while $[B]$ denotes the matrix containing derivatives of the shape function and $\{\delta\}^{\mathrm{e}}$ denotes the nodal displacement vector.

The temperature increase within an element is represented as:

$$\Delta T = \sum_{i=1}^{8} N_i^{\mathrm{e}} T_i^{\mathrm{e}} - T_0 \tag{42}$$

We can also write:

$$\{\nabla w\} = [\mathrm{B}]\ \{w\}^{\mathrm{e}}\ (\text{Galerkin scheme}) \tag{43}$$

where the elements' nodal weights are denoted by $\{w\}^{\mathrm{e}}$.

Substituting Equation (40) and Equation (43) in a weighted integral expression of equilibrium Equation (39):

$$\sum_{e=1}^{ne}\{\mathrm{w}\}^{eT}[STK]^e\{\delta\} = \sum_{e=1}^{ne}\{\mathrm{w}\}^{eT}\{stf\}^e \tag{44}$$

where *ne* is the no. of area element, $[STK]^{\mathrm{e}}$ is the elemental coefficient matrix for stress and $\{stf\}^{\mathrm{e}}$ is the elemental force vector

$$[stf]^e = \int[B]^{\mathrm{T}}\{m\}2\pi r\mathrm{d}r\mathrm{d}z \tag{45}$$

$$[STK]^e = \int_{\Omega^e}[B]^{\mathrm{T}}[D][B]2\pi r\mathrm{d}r\mathrm{d}z \tag{46}$$

The Gauss quadrature integration technique 3 × 3 is applied to solve the above integrals Equation (45) and Equation (46). We can also write assembled finite elemental equations as

$$[GK]\{GU\} = \{GF\} \tag{47}$$

The global nodal displacement vector is denoted by $\{GU\}$, the global right-side vector by $\{GF\}$ and the global coefficient matrix by $[GK]$. The Gauss elimination method is applied to the aforementioned Equation (47) to calculate the nodal displacement after boundary conditions are applied.

The solution of Equation (47) is obtained in terms of nodal displacement. The thermal stress is calculated by nodal displacement and temperature distribution as input by Equation (11) and (40). Equation (22) is used to compute the equivalent stress, which is then compared to the yield stress to determine whether yielding occurs. The process of comparison is carried out for all the elements.

4 RESULT AND DISCUSSION

A FEM-based model was developed for the thermal stress analysis of the work piece in EDM. For validation, the temperature distribution of the present model is compared with numerical results of Yadav et al.[1] and Shankar et al.[13] having the same process conditions. In the present model, the temperature distribution is determined using a Gaussian heat-flux distribution with an energy partition R_w value of 0.08. Different process parameters were used by researchers for thermo-mathematical modeling of EDM.[1–26] The material properties and process parameters used in the present model are given in **Table 1**.

Table 1: Material properties and process parameters used in this model

Material	AISI A2 Die Steel
C/(J/kg)	460.0
E/(GN/m^2)	190
h_c/(W/m^2·K)	10,500
I/A	9
K/(W/m·K)	26
R/μm	125
R_w	0.08
T_m/K	1697
T_0/K	298
U_b/(V)	40
ρ/(kg/m^3)	7750

Figure 2 shows the variation of the top surface temperature distribution for the Gaussian heat source along the radial direction from the center. The temperature profile along the radial axis is parabolic in nature.

The comparison of the temperature distribution with the result of Yadav et al. and Shankar et al. is shown in

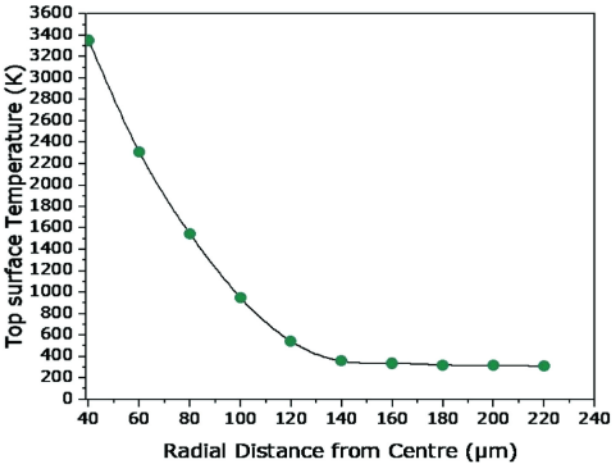

Figure 2: Temperature variation along radial axis

Figure 3.[1,13] Outside the spark radius, there is substantial agreement. One of the reasons for the quantitative discrepancy in the spark radius zone is a variation in the heat-flux profiles adopted. The Gaussian heat source, which is considered to be more realistic, exhibits severe temperature gradients inside the spark radius region. These steep gradients are found to be the major cause of thermal stresses in the workpiece.

The thermal stress components are calculated for each of the Gaussian integrating points within each discretized domain element. All Gauss points at the top surface of the considered domain and element size are discovered to be 7 μm, well below the top layer of the domain. Likewise, all Gauss points near the center line of the spark are discovered to be 7 μm far from the center line. As a result, typical planes near the spark are selected to show the results of stress distributions along the radial distance and depth for simulation results

Figure 4 and **Figure 6** show that the variation of the thermal stresses component along the radial distance in AISI A2 die steel workpiece at 7 μm below the top surface. Because of the constraint from the material that expands less, a compressive stress area is detected around the spark center point ($r = 0$). A section of the workpiece material under a spark expands more considerably owing to the higher temperature rise, causing compressive stresses. The radial component (σ_{rr}) is found to be the highest with an approximate value of 2700 MPa, closely followed by the tangential component ($\sigma_{\theta\theta}$) with approximate value of 2650 MPa, followed by an axial/vertical component (σ_{zz}) is only about 700 MPa. The shear component (σ_{rz} = 150 MPa) is substantially less than the other three components (σ_{rr}, σ_{zz}, $\sigma_{\theta\theta}$) and its sign shifts somewhat away from the spark's center. Beyond 400 μm from the center, almost no thermal stresses are found.

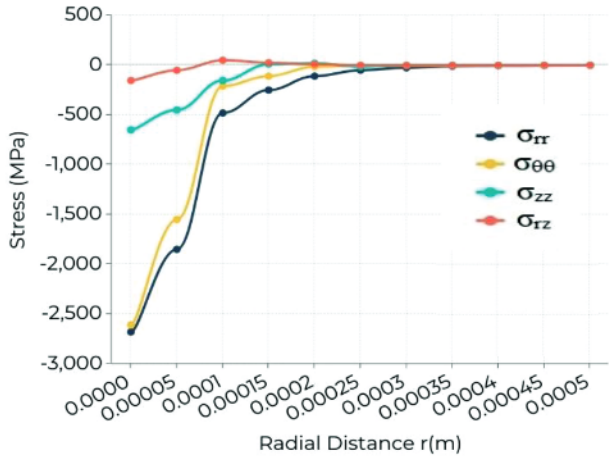

Figure 4: Variation of thermal stress component in AISI A2 die steel workpiece for U_b = 40 V, I = 9 A, T_{on} = 100 μs, T_{off} = 100 μs, duty cycle = 50 % along radial distance at r = 7 μm from the top surface

Figure 5 and **Figure 7** show the variation of the thermal stresses' component down the depth in an AISI A2 die steel workpiece about 7 μm below the top surface. In almost all cases, the stress fields are tensile in nature. These curves also illustrate that the undesirable thermal tensile stresses are critical near the top surface. They

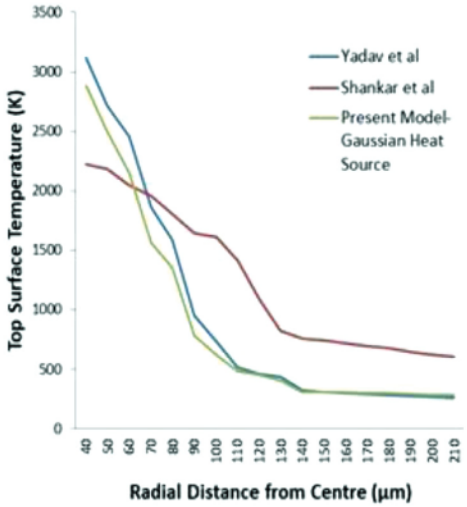

Figure 3: Comparison of top surface temperature and variation along radial axis with Yadav et al. and Shankar et al.[1,13]

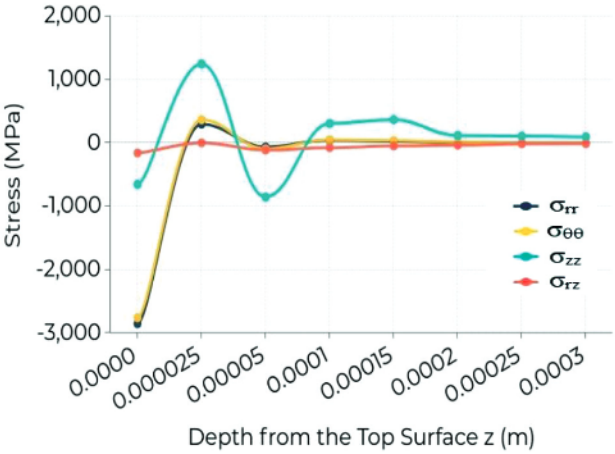

Figure 5: Variation of thermal stress component in AISI A2 die steel workpiece for U_b = 40 V, I = 9 A, T_{on} = 100 μs, T_{off} = 100 μs, duty cycle = 50 % along depth at r = 7 μm from the top surface

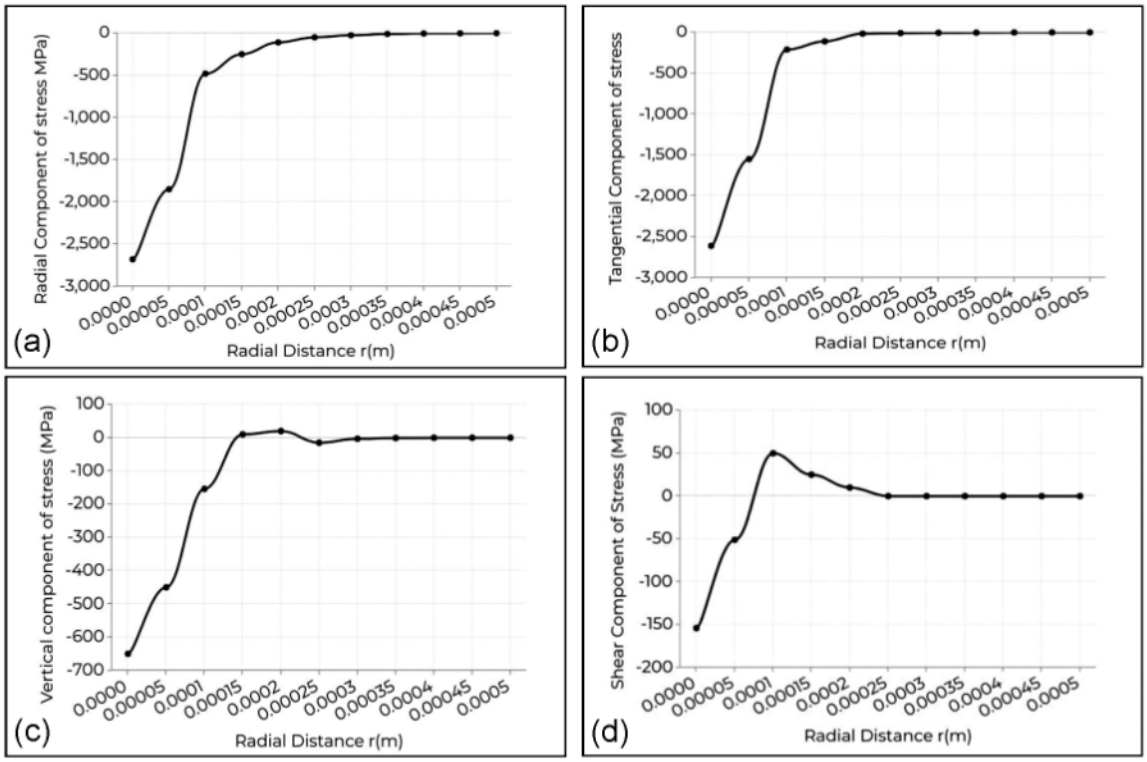

Figure 6: Variation along radial distance; a) radial component of thermal stress (σ_{rr}), b) tangential component of stress ($\sigma_{\theta\theta}$) c) axial/vertical component of stress (σ_{zz}), d) shear component of stress (σ_{rz})

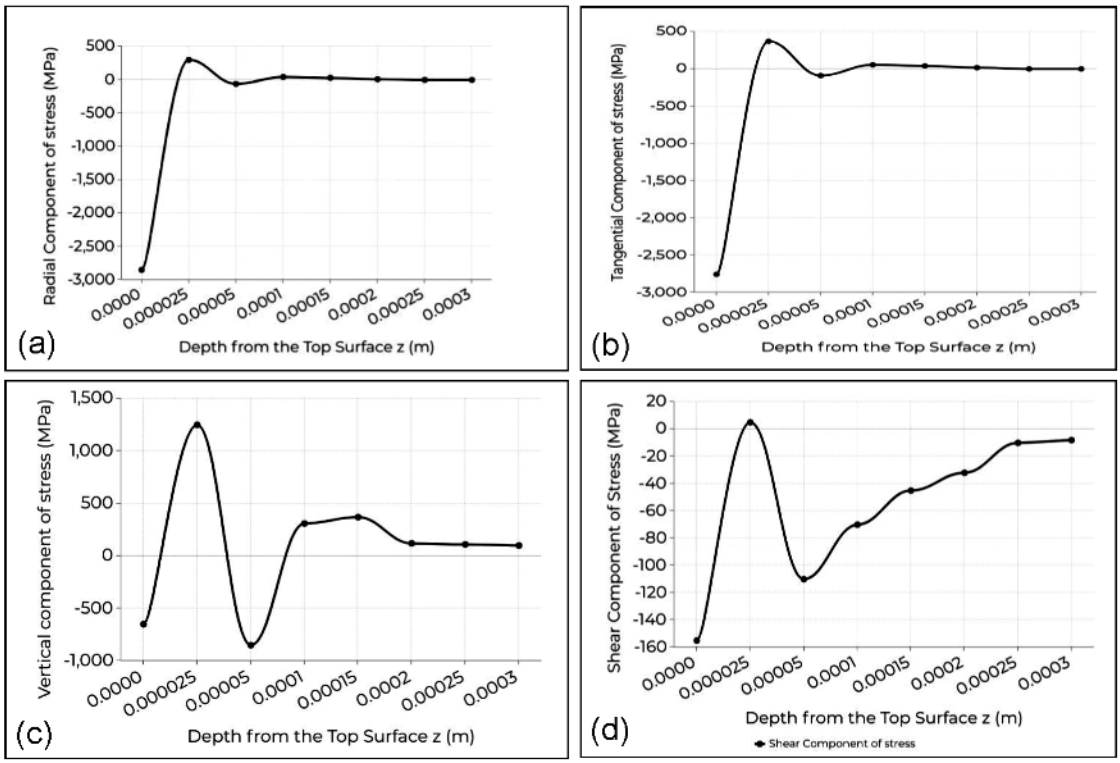

Figure 7: Variation along radial distance: a) radial component of thermal stress (σ_{rr}), b) tangential component of stress ($\sigma_{\theta\theta}$), c) axial/vertical component of stress (σ_{zz}), d) shear component of stress (σ_{rz})

fluctuate up to 100 µm, but slowly drop to zero beyond 300 µm. The most critical component is axial/vertical σ_{zz} that fluctuates within 100 µm depth from –750 MPa to 1250 MPa. This demonstrates that σ_{zz} causes huge residual thermal stress close to the top surface.

5 CONCLUSION

In the present study, numerical simulations were carried out with a final element-based code for predicting the temperature distribution and thermal stress fields after a single spark of EDM in an AISI A2 steel workpiece. In developing the model, the important characteristics of the process are considered, for example, temperature-dependent material properties, the size and shape of heat source (Gaussian heat source), the percentage fraction of the heat input to the workpiece, the pulse time on/off. The temperature profile and thermal stress distribution around a single spark that occur in the work piece material as a result of high temperature, deformations, and transient operation are analyzed. The temperature rises sharply during the heating cycle and then drops rapidly during the quenching cycle. Thermal compressive stresses are observed beneath the crater, while tensile stresses appear away from the axis of symmetry. After one spark, significant compressive and tensile stresses are observed in a thin layer around the spark location. Thermal stresses are also observed to exceed the workpiece's yield strength in a very thin area near the spark. The findings provided insight into the potentially hazardous nature of thermal stresses generated during EDM.

6 REFERENCES

[1] V. Yadav, V. K. Jain, P. M. Dixit, Thermal stresses due to electrical discharge machining, International Journal of Machine Tools and Manufacture, 42 (**2002**) 8, 877–888, doi:10.1016S0890-6955(02)00029-9

[2] J. P. Kruth, L. Stevens, L. Froyen, B. Lauwers, Study of the White Layer of a Surface Machined by Die-Sinking Electrical-Discharge Machining, CIRP Annals, 44 (**1995**) 1, 169–172, doi:10.1016/S0007-8506(07)62299-9

[3] M. Field, J. F. Khales, Review of surface integrity of machined component, Annals of CIRP, 25 (**1976**) 2, 569–573

[4] A. Klink, Y. B. Guo, F. Klocke, Surface integrity evolution of powder metallurgical tool steel by main cut and finishing trim cuts in wire-EDM, Procedia Engineering, 19 (**2011**), 178–183, doi:10.1016/j.proeng.2011.11.098

[5] M. Antar, S. Soo, D. Aspinwall, M. Cuttell, R. Perez, A. Winn, WEDM of aerospace alloys using žCleanCut' generator technology, ISEM XVI, Shanghai, (2010), 285–290

[6] M. T. Antar, S. L. Soo, D. K. Aspinwall, C. Sage, M. Cuttell, R. Perez, A. J. Winn, Fatigue response of Udimet 720 following minimum damage WEDM, Materials & Design, 42 (**2012**), 295–300, doi:10.1016/j.matdes.2012.06.003

[7] A. Erden, A. Faruk, K. Murat, Comparison of mathematical models for electric discharge machining, Journal of Materials Processing and Manufacturing Science, 4 (**1995**), 163–176

[8] F. Roethel, L. Kosec, V. Garbajs, Contribution to the microanalysis of the spark eroded surfaces, Annals of CIRP 25 (1975), 135–140

[9] L. C. Lee, L. C. Lim, V. Narayanan, V. V. Venkatesh, Quantificiation of surface damage of tool steels after EDM, Int. J. Mach. Tools Manufact., 28 (**1988**) 4, 359–372

[10] K. P. Rajurkar, S. M. Pandit, Quantification expressions for some aspects of surface integrity of electrical-discharge machined components, Trans. ASME, Journal of Engineering for Industry, 106 (**1984**), 171–177

[11] A. Erden, B. Kaftanoglu, Heat transfer modeling of electric discharge machining, 21st MTDR Conference, Swansea, 1980, 351–358

[12] S. T. Jilani, P. C. Pandey, Analysis and modeling of EDM parameters, Precision Engineering, 4 (**1982**) 4, 215–221

[13] P. Shankar, V. K. Jain, T. Sundarajan, Analysis of spark profiles during EDM process, Machining Science and Technology, 1 (**1997**) 2, 195–217

[14] S. V. Shanmugam, V. Krishnaraj, K. A. Jagdeesh, S. V. Kumar, S. Subash, Numerical Modelling of Electrical-Discharge Machining Process Using Moving Mesh Feature, Procedia Engineering, 64 (**2013**), 747–756, doi:10.1016/j.proeng.2013.09.150

[15] A. Erden, Effect of materials on the mechanism of electric discharge machining (EDM), Trans. ASME, Journal of Engineering Materials and Technology, 108 (**1983**), 247–251

[16] R. Snoyes, F. V. Dijck, Plasma channel diameter growth affects stock removal, Annals of CIRP 21 (1972) 1, 39–40

[17] P. C. Pandey, S. T. Jilani, Plasma channel growth and the resolidified layer in EDM, Precision Engineering 8 (1986) 2, 104–110

[18] P. Madhu, V. K. Jain, T. Sundarajan, K. P. Rajurkar, Finite element analysis of EDM process, Processing of Advanced Materials 1 (**1991**), 161–173

[19] R. Bhattacharya, V. K. Jain, P.S. Ghosh, Numerical simulation of thermal erosion in EDM process, IE (I) Journal-PR, 77 (**1996**) 13–19

[20] D. D. DiBitonto, P. T. Eubank, M. R. Patel, A. Barrufet, Theoretical models of the electrical discharge machining process—I: a simple cathode erosion model, Journal of Applied Physics, 66 (**1989**) 9, 4095–4103, doi:10.1063/1.343994

[21] M. R. Patel, A. Barrufet, P. T. Eubank, D. D. DiBitonto, Theoretical models of the electrical discharge machining process—II: the anode erosion model, Journal of Applied Physics 66 (1989) 9, 4104–4111, doi:10.1063/1.343995

[22] R. Butola, Q. Murtaza, R. Singari, An experimental and simulation validation of residual stress measurement for manufacturing of friction stir processing tool. Indian Journal of Engineering and Materials Sciences, 27 (**2020**), 826–836, http://nopr.niscair.res.in/handle/123456789/55687

[23] D. Kumar, K. Kumar, H. S. Payal, K. K. S. Mer, Mathematical modeling and analysis of productive aspects in Electrical Discharge Machining of AISI A2 steel, Materials Today: Proceedings, 5 (**2018**) 11, 24691–24701, doi:10.1016/j.matpr.2018.10.267

[24] R. Butola, N. Choudhary, R. Kumar, P. K. Mouria, M. Zubair, R. M. Singari, Measurement of residual stress on H13 tool steel during machining for fabrication of FSW/FSP tool pins, Materials Today: Proceedings, 43 (**2021**) 1, 256–262, doi:10.1016/j.matpr.2020.11.656

[25] K. Bector, M. Singh, D. Pandey, R. Butola, R. M. Singari, Study of residual stresses in multi-pass friction stir processed surface composites, Advances in Materials and Processing Technologies, (2021), doi:10.1080/2374068X.2021.1939983

[26] R. Butola, P. Chandra, K. Bector, R. Singari, Fabrication and multi-objective optimization of friction stir processed aluminium based surface composites using Taguchi approach, Surface Topography: Metrology and Properties, 9 (**2021**), doi:10.1088/2051-672X/ac0ba3